High-Frequency Resonance Damping of DFIG-Based Wind Power System Under Weak Network

Yipeng Song, Xiongfei Wang, *Member, IEEE*, and Frede Blaabjerg, *Fellow, IEEE*

***Abstract*—When operating in a micro or weak grid which has a relatively large network impedance, the doubly fed induction generator (DFIG)-based wind power generation system is prone to suffer high-frequency resonance due to the impedance interaction between the DFIG system and the parallel compensated network (series *RL* + shunt *C*). In order to improve the performance of the DFIG system as well as other units and loads connected to the weak grid, the high-frequency resonance needs to be effectively damped. In this paper, the proposed active damping control strategy is able to implement effective damping either in the rotor-side converter or in the grid-side converter, through the introduction of virtual positive capacitor or virtual negative inductor to reshape the DFIG system impedance and mitigate the high-frequency resonance. A detailed theoretical explanation on the virtual positive capacitor or virtual negative inductor has been given, and their parameters are also optimally designed. The proposed DFIG system damping control strategy has been validated by experimental results.**

***Index Terms*—Doubly fed induction generator (DFIG) system impedance, high-frequency resonance damping, series *RL* + shunt *C* network, virtual negative inductor, virtual positive capacitor.**

I. Introduction

As the renewable power generation continues to increase worldwide, the penetration of wind energy, solar energy, etc., into the microgrid or weak grid is becoming more and more popular. Among the different kinds of renewable power generation units, the doubly fed induction generator (DFIG)-based wind power generation has been widely implemented due to its performance advantages of a smaller converter rating around 30% of the generator rating, variable speed and four-quadrant active and reactive power operation capabilities, lower converter cost, and power losses [1]–[6].

So far, the increasing number of renewable power generation units has been connected to the distributed weak network whose network impedance is much larger than the traditional large-scale stiff power grid. As a consequence, the impedance interaction between the renewable power generation units (e.g., grid-connected converter for solar energy, DFIG-based wind turbine system) and the weak network requires careful considerations. Two kinds of resonances have been investigated in the previous works, i.e., the subsynchronous resonance (SSR) of the DFIG system [7]–[14] and high-frequency resonance in the grid-connected converter [15]–[23].

Manuscript received January 11, 2016; revised March 30, 2016; accepted April 14, 2016. Date of publication April 20, 2016; date of current version December 9, 2016. Recommended for publication by Associate Editor P. Bauer.

The authors are with the Department of Energy Technology, Aalborg University, Aalborg 9220, Denmark (e-mail: yis@et.aau.dk; xwa@et.aau.dk; fbl@et.aau.dk).

Color versions of one or more of the figures in this paper are available online at http://ieeexplore.ieee.org.

Digital Object Identifier 10.1109/TPEL.2016.2555846

On one hand, the SSR phenomenon between the DFIG system and series compensated weak network has been well investigated based on the detail impedance modeling of DFIG system in [7]–[14]. The harmonic linearization method is employed to obtain the positive and negative impedance sequences of DFIG system in [7]–[10], especially the influence of PI regulator parameters in the rotor current closed-loop control and phase-locked loop control is studied concerning the SSR, and the DFIG SSR under different rotor speed is also investigated in [7]–[10]. Besides, the overall equivalent circuit modeling of the DFIG system and series compensated weak network is reported in [11], and it is concluded that the interaction between the electric network and the converter controller is a leading cause of the SSR phenomena. The design of auxiliary SSR damping controller and selection of control signals in the DFIG converters are demonstrated in [14] in order to effectively mitigate the SSR.

On the other hand, as for the grid-connected converter, many effective resonance damping strategies for the high-frequency resonance have been reported in [15]–[24]. The active damping of high-frequency resonance as well as the mitigation of harmonic distortion in the grid-connected converter is well investigated in [15]–[24]. The converter with series *LC* filter, rather than the traditional *LCL* filter, is studied to achieve the active damping in [16]. The virtual *RC* impedance is introduced in [18] and [19], i.e., positive resistance to achieve better performance of harmonic resonance damping; while negative inductance to achieve better performance of harmonic distortion mitigation by reducing the grid-side inductance. The unknown resonance frequency is first identified by cascaded adaptive notch filter (ANF) structure in [22], then the active damping can be implemented based on the detected resonance frequency. An overview of the virtual impedance-based active damping strategy for the grid-connected voltage-source and current-source converters are summarized in [23], and several alternative methods of implementing the virtual impedance are concluded. Importantly, the interaction coupling between two converters connected to the same point–of-common coupling (PCC) or different point of coupling via nonideal grid is discussed in [24], and the bifurcation boundaries are also derived. Since the converter control parameters may influence its stability, a systematic design method of the controller parameter is given based on the chosen *LCL* filter resonance frequency in [25] and [26].

Thus, it can be found that the DFIG SSR and grid-connected converter high-frequency resonance damping have been completely well investigated, while the case of DFIG high-frequency resonance and its effective damping control strategy is never investigated before. In this paper, the active damping control

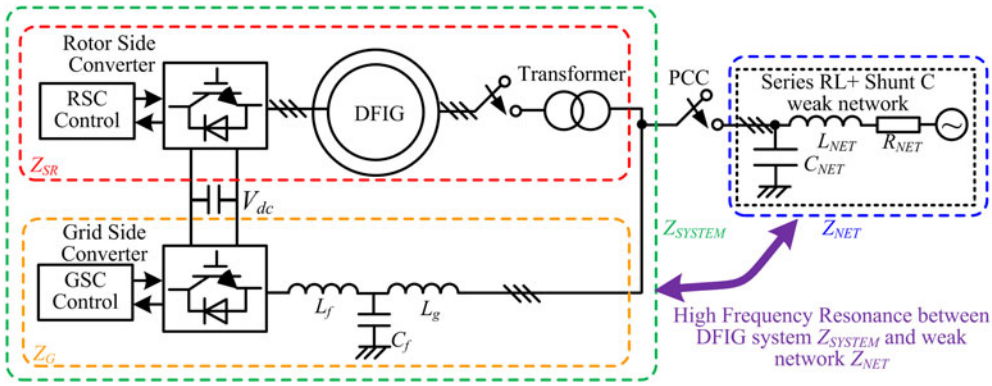

Fig. 1. Configuration diagram of the DFIG system and series *RL* + shunt *C* weak network.

strategy of the DFIG system high-frequency resonance will be explored in detail, with the introduction of positive capacitor (PC) or negative inductor (NL) as a virtual impedance, so as to reshape the DFIG system impedance and damp the high-frequency resonance.

It should be noted that the series compensated network consisting of resistor, inductor, capacitor, (*RLC*) in series is taken into consideration in the DFIG SSR analysis in [7]–[14], while the other types of network, e.g., series *RL*, series *RL* + shunt *C*, are not investigated concerning the DFIG system, but only discussed concerning the grid-connected converter active damping in [15]–[26]. Besides, the DFIG GSC filter in [7]–[14] adopts *L* filter; however, in the practical application where large power scale DFIG turbine around MW is widely implemented, the GSC filter always adopts the *LCL* filter due to its better switching harmonics filtering performance than the *L* filter.

This paper is organized as follows. The impedance modeling of DFIG machine and RSC, together with the impedance modeling of GSC and *LCL* filter, is established first in Section II. The high-frequency resonance between DFIG system and the parallel compensated network (series *RL* + shunt *C*) is theoretically analyzed in Section III. The proposed active damping control strategy with the introduction of PC or NL as virtual impedance in either RSC or GSC is demonstrated in Section IV. The parameters design of the virtual impedance and the control block diagram are given out in Section V. The proposed active damping strategy of DFIG system high-frequency resonance is validated by experimental results in Section VI. Finally, the conclusion is given in Section VII.

II. DFIG System Impedance Modeling

The DFIG system impedance modeling has been well established in [7]–[14], nevertheless since the impedance modeling serves as a foundation for the active damping strategy, the DFIG system impedance modeling still needs to be described here. Importantly, the *LCL* filter with better switching harmonics filtering performance, rather than the *L* filter in [7]–[14], is adopted in this paper. Besides, the mutual inductance and the digital control delay of 1.5 sample period [15] caused by the voltage/current sampling and pulse width modulation (PWM) update are taken into consideration in the impedance modeling in this paper.

TABLE I
Parameters of RSC, DFIG Machine, GSC, and *LCL* Filter

Rated Power	7.5 kW	Voltage Level	400 V
L_g	7 mH	L_f	11 mH
C_f	6.6 μF	L_m	79.3 mH
$L_{\sigma s}$	3.44 mH	$L_{\sigma r}$	5.16 mH
R_s	0.44 Ω	R_r	0.64 Ω
K_{prsc}	8	K_{irsc}	16
K_{pgsc}	8	K_{igsc}	16
ω_r	0.8 p.u.	T_d	150 μs
f_s	10 kHz	f_{sw}	5 kHz

A. General Description of the Investigated DFIG System

Fig. 1 shows the configuration diagram of the DFIG system and series *RL* + shunt *C* weak grid, the parameters of the DFIG system are available in Table I. As it can be seen, the RSC controls the rotor voltage to deliver the stator output active and reactive power, GSC is responsible for maintaining stable dc-link voltage, and the *LCL* filter is adopted due to better switching harmonic filtering performance. For the purpose of preventing grid connection inrush current and inner system current circulation, a transformer is connected between DFIG stator winding and PCC. The transformer does not change the voltage level between primary and secondary side; thus, it will be neglected during the impedance modeling in following discussion.

The parallel compensated weak network with the configuration of series *RL* + shunt *C* is connected to the PCC. The high-frequency resonance will occur through the impedance interaction between DFIG system and parallel compensated weak network, the detailed theoretical analysis can be found in following discussion.

B. GSC and LCL Filter Impedance Modeling

As shown in Fig. 2, the grid side of the DFIG system contains the GSC and the *LCL* filter. Based on [11], the impedance modeling of GSC and *LCL* filter can be presented in Fig. 3, where $G_c(s-j\omega_0)$ is the PI current controller, $G_d(s-j\omega_0)$ is the digital control delay of 1.5 sample period. Note that ω_0 is the grid network fundamental component angular speed of

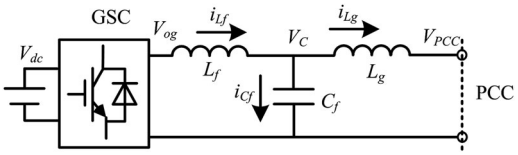

Fig. 2. Circuit of GSC and *LCL* filter.

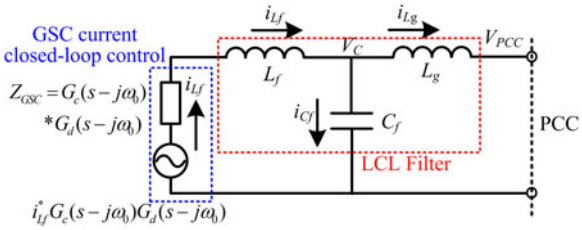

Fig. 3. Impedance modeling of GSC and *LCL* filter.

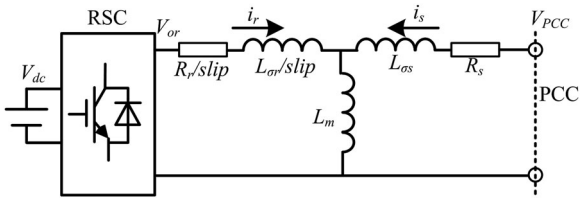

Fig. 4. Circuit of rotor-side converter and DFIG machine.

100π rad/s, it is introduced due to the implementation of PI closed-loop current regulation in the synchronous frame.

Normally, the GSC control has the outer control loop of the dc-link voltage; however, since the dc-link voltage has much longer time constant, the control bandwidth of the dc-link voltage is lower than 100 Hz, thus the impedance modeling of the dc-link voltage control loop in the GSC is neglected.

Thus, as given in Fig. 3, the GSC current closed-loop control is modeled as one voltage source $i_{\mathrm{Lf}}^{*}G_c(s-j\omega_0)G_d(s-j\omega_0)$ in series connection with one impedance $Z_{\mathrm{GSC}}=G_c(s-j\omega_0)G_d(s-j\omega_0)$.

According to the impedance theory, the impedance of the GSC and *LCL* filter seen from the PCC can be obtained by setting the voltage source to zero, then the impedance of the DFIG grid side (including GSC and *LCL* filter) can be deduced as

$$Z_G=\frac{Z_{\mathrm{Cf}}\left(Z_{\mathrm{Lf}}+Z_{\mathrm{GSC}}\right)+Z_{\mathrm{Lg}}\left(Z_{\mathrm{Lf}}+Z_{\mathrm{GSC}}\right)+Z_{\mathrm{Cf}}Z_{\mathrm{Lg}}}{Z_{\mathrm{Cf}}+\left(Z_{\mathrm{Lf}}+Z_{\mathrm{GSC}}\right)} \tag{1}$$

where, $Z_{\mathrm{GSC}}=G_c(s-j\omega_0)G_d(s-j\omega_0)$, $Z_{\mathrm{Cf}}=1/sC_f$, $Z_{\mathrm{Lf}}=sL_f, Z_{\mathrm{Lg}}=sL_g$.

C. RSC and Machine Impedance Modeling

Fig. 4 shows the circuit of the RSC and DFIG machine. Since the rotor current control and output voltage are both calculated in the rotor stationary reference frame, they need to be rotated back to the stationary frame by the slip angular speed expressed as [7]–[10]

$$\mathrm{slip}=(s-j\omega_r)/s \tag{2}$$

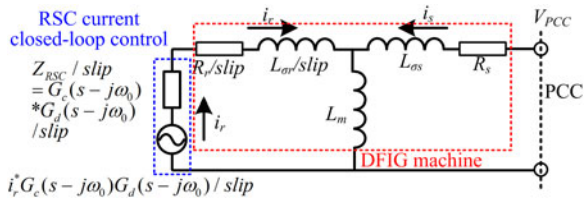

Fig. 5. Impedance modeling of rotor-side converter and DFIG machine.

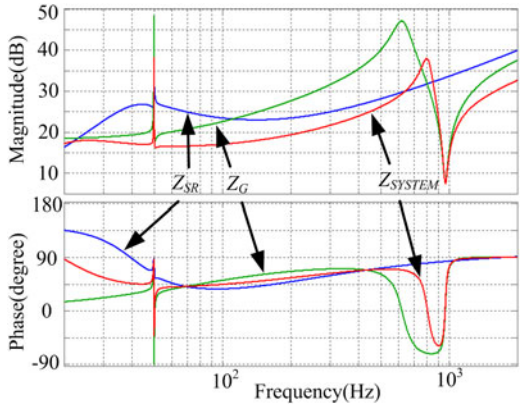

Fig. 6. Bode diagram of RSC and DFIG machine impedance Z_{SR}, GSC and *LCL* filter impedance Z_G, and DFIG system impedance Z_{SYSTEM}.

where ω_r is the rotor electric angular speed.

Similar as the GSC and *LCL* filter, the impedance modeling of RSC and DFIG machine can be obtained as shown in Fig. 5.

By setting the rotor control voltage source to zero, the impedance of the RSC and DFIG machine seen from the PCC can be obtained as

$$Z_{\mathrm{SR}}=\frac{Z_{\mathrm{Lm}}H/\mathrm{slip}+\left(R_s+Z_{L\sigma s}\right)H/\mathrm{slip}+Z_{\mathrm{Lm}}\left(R_s+Z_{L\sigma s}\right)}{Z_{\mathrm{Lm}}+H/\mathrm{slip}} \tag{3}$$

where, $H=R_r+Z_{L\sigma r}+Z_{\mathrm{RSC}}, Z_{\mathrm{RSC}}=G_c(s-j\omega_0)G_d(s-j\omega_0), Z_{\mathrm{Lm}}=sLm, Z_{L\sigma r}=sL_{\sigma r}, Z_{L\sigma r}=sL_{_{\sigma r}}$.

D. DFIG System Impedance

As shown in Fig. 1, the rotor part (RSC and DFIG machine) and grid part (GSC and *LCL* filter) are connected in parallel to the PCC. Thus, the DFIG system impedance can be derived based on (1) and (3) as

$$Z_{\mathrm{SYSTEM}}=\frac{Z_G Z_{\mathrm{SR}}}{Z_G+Z_{\mathrm{SR}}} \tag{4}$$

The Bode diagrams of RSC and DFIG machine impedance Z_{SR}, GSC and *LCL* filter impedance Z_G, and DFIG system impedance Z_{SYSTEM} are drawn in Fig. 6. The parameters used to plot the Bode diagram are given in Table I.

As it can be observed from Fig. 6, within the lower frequency range, both the RSC and DFIG machine impedance Z_{SR} and GSC and *LCL* filter impedance Z_G have a high peak at 50 Hz due to the rotation of the reference frame from synchronous frame to stationary frame, thus the DFIG system impedance Z_{SYSTEM} also has the high peak at 50 Hz.

As for the higher frequency range (e.g., above 500 Hz), the $Z_{\rm SR}$ behaves almost as an inductive unit with the phase response about 90°. The Z_G has one magnitude peak around 620 Hz and one magnitude concave around 966 Hz caused by the *LCL* filter. It needs to point out the phase response of Z_G from 620 and 966 Hz is capacitive below 0°, which is quite different from the $Z_{\rm SR}$.

The DFIG system impedance $Z_{\rm SYSTEM}$ has a similar magnitude and phase response as the Z_G. However, due to the involvement of $Z_{\rm SR}$, the $Z_{\rm SYSTEM}$ magnitude peak shifts from 620 to 803 Hz, and the phase response within the range of 803 to 966 Hz is also lifted up, which is helpful to avoid the high-frequency resonance (will be explained in following sections).

III. High-Frequency Resonance Between DFIG System and Parallel Compensated Network

As explained in Fig. 6, the DFIG system behaves inductive with phase response of 90° at high frequency (>1 kHz); thus, in order to make the high-frequency resonance to happen, the weak network should behave capacitive with the phase response of −90° at the high frequency, thus the phase difference of 180° will be produced to cause the high-frequency resonance. From this point of view, the following discussion on the high-frequency resonance between DFIG system and weak network will be conducted on the assumption of parallel compensated weak network, i.e., series *RL*+ shunt *C* network.

While for the series *RL* network which behaves inductive in the entire frequency range, it is impossible to make the high-frequency resonance to occur because of almost zero phase difference between series *RL* weak network and DFIG system. For the series compensated network, i.e., series *RLC* network in [7]–[14], its phase response at high frequency is identical to series *RL* network, resulting in no high-frequency resonance as well. Thus, the weak network configuration of series *RL* and series *RLC* will not be discussed in this paper.

Obviously, the impedance of the series *RL* + shunt *C* network can be presented as

$$Z_{\rm NET\_RL\_C} = \frac{(sL_{\rm NET} + R_{\rm NET})\frac{1}{sC_{\rm NET}}}{sL_{\rm NET} + R_{\rm NET} + \frac{1}{sC_{\rm NET}}} \tag{5}$$

where $R_{\rm NET}$ and $L_{\rm NET}$ are the network series resistance and inductance and $C_{\rm NET}$ is the network shunt capacitance.

The following equation can be obtained by rewriting the impedance of series *RL* + shunt *C* network in (5)

$$Z_{\rm NET\_RL\_C} = \frac{\frac{1}{C_{\rm NET}}s + \frac{R_{\rm NET}}{L_{\rm NET}C_{\rm NET}}}{s^2 + \frac{R_{\rm NET}}{L_{\rm NET}}s + \frac{1}{L_{\rm NET}C_{\rm NET}}}. \tag{6}$$

It can be observed from (6) that the magnitude peak of the network impedance is determined by $L_{\rm NET}$ and $C_{\rm NET}$. In this paper, the $L_{\rm NET}$ is assumed to be constant, while the $C_{\rm NET}$ will vary according to different compensation level; thus, resulting in the network impedance peak to shift within certain frequency range.

As shown in Fig. 6, the phase response of the DFIG system impedance is close to 90° at the frequency higher than 1 kHz. Therefore, the high-frequency resonance is most likely to happen within the frequency range higher than 1 kHz, this will be described in details in the following discussion.

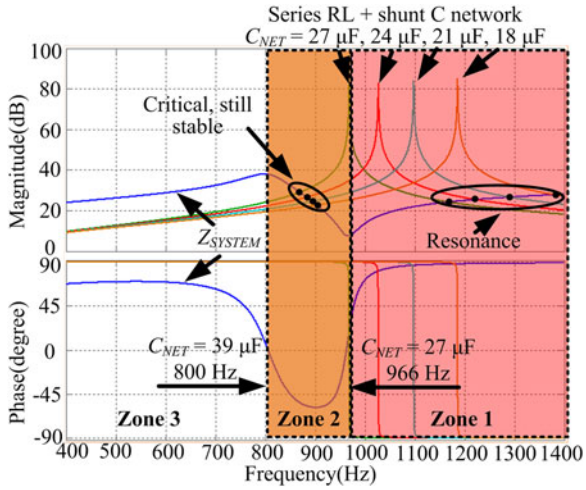

Fig. 7. Bode diagram of a DFIG system impedance and series *RL* + shunt *C* network impedance with $C_{\rm NET}$ smaller than 27 μF (27, 24, 21, 18 μF), $R_{\rm NET} = 3$ mΩ, $L_{\rm NET} = 1$ mH.

Fig. 7 shows the Bode diagram of the DFIG system impedance and series *RL* + shunt *C* network impedance with $C_{\rm NET}$ smaller than 27 μF (27, 24, 21, 18 μF). As shown clearly, the network impedance and DFIG system impedance have several magnitude intersection points both in Zone 2 and Zone 1.

For the intersection points located within Zone 2, the phase differences are from 135° to 149°, indicating that the resonance from 800 to 966 Hz is less likely to happen due to an acceptable phase margin, and the DFIG system can still work stable. On the other hand, for the intersection points located within Zone 1, the phase differences are always 180° for all the four cases of different capacitances, indicating that the high-frequency resonance of 1160, 1220, 1290, and 1380 Hz will occur, respectively, for the shunt capacitor $C_{\rm NET}$ of 27, 24, 21, 18 μF.

IV. Proposed Active Damping Strategy for a DFIG System

As illustrated in the previous section, the high-frequency resonance of 1220 Hz will happen if the DFIG system parameters are as listed in Table I, and the parallel compensated weak network parameters are chosen as $C_{\rm NET} = 24$ μF, $R_{\rm NET} = 3$ mΩ, $L_{\rm NET} = 1$ mH. In order to effectively damp the resonance, the virtual PC or NL needs to be employed as explained in this section.

A. DFIG System Impedance Reshaping Through RSC

As it can be seen from Fig. 7, for the sake of mitigating the high-frequency resonance, the phase difference between the DFIG system and weak network needs to be reduced, obviously a concave in the phase response of the DFIG system is preferred. Since the DFIG system behaves inductive at the high-frequency range, the virtual PC or NL is preferred due to their negative phase character.

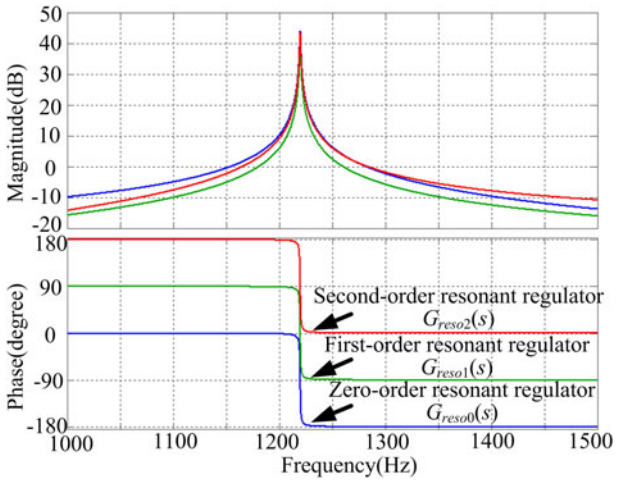

Fig. 8. Bode diagram of zero-order, first-order, and second-order resonant regulator.

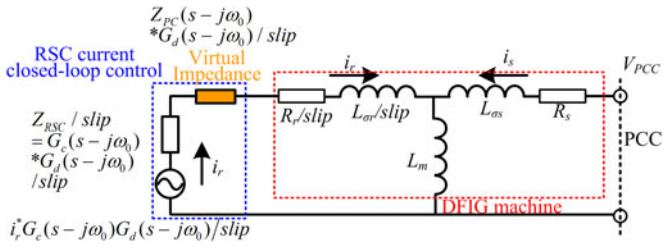

Fig. 9. Impedance modeling of RSC and DFIG machine with the introduction of virtual impedance.

In order to reshape the magnitude and phase response at only the resonance frequency rather than the entire frequency range, the resonant regulator can be employed due to its significant frequency selection capability [18]

$$G_{\text{reso0}}(s) = \frac{k_0}{s^2 + \omega_c s + \omega_{\text{reso}}^2} \tag{7a}$$

$$G_{\text{reso1}}(s) = \frac{k_1 s}{s^2 + \omega_c s + \omega_{\text{reso}}^2} \tag{7b}$$

$$G_{\text{reso2}}(s) = \frac{k_2 s^2}{s^2 + \omega_c s + \omega_{\text{reso}}^2}. \tag{7c}$$

The Bode diagrams of three different resonant regulators, i.e., zero-order, first-order, and second-order resonant regulator, are plotted in Fig. 8, and their transfer function presented in (7). As shown, the phase response changes from 0° to −180° for zero-order resonant regulator, 90° to −90° for first-order resonant regulator, and 180° to 0° for second-order resonant regulator, respectively. This inherent character, i.e., phase response changing 180° at the tuned resonant frequency, obviously results in the opposite signs of the virtual impedance. For instance, when the PC and the zero-order resonant regulator are employed, the introduced capacitor will behave as PC due to the 0° phase response within the frequency range lower than resonant frequency, while behaves as a negative capacitor due to the 180° phase response within the frequency range higher than resonant frequency. The other cases can be similarly deduced.

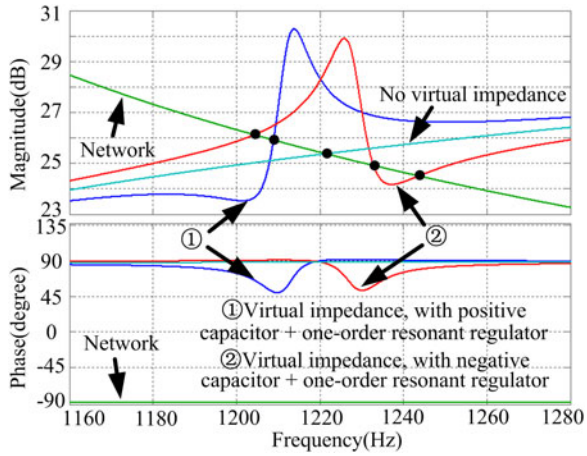

Fig. 10. Bode diagram of a DFIG system impedance considering the proposed virtual impedance Z_{PC} with positive capacitor and first-order resonant regulator, $\omega_c = 5$ rad/s, $\omega_{\text{reso}} = 2\pi * 1220$ rad/s, $C_{\text{xrsc}} = 0.08$ μF, control delay = 150 μs.

Considering that the parallel compensated network has impedance shape of gradual decreasing magnitude as shown in Fig. 7, when the high-frequency resonance frequency is higher than 1 kHz, the reshaped impedance of the DFIG system is preferred to first decrease when lower than the resonance frequency, then increase when higher than the resonance frequency. By reshaping the DFIG system impedance like this, it can be ensured that only one magnitude intersection point, rather than three points exists, and helps to reduce the possibility of high-frequency resonance. The reason for reshaping the DFIG system impedance like this will be further explained in Fig. 10.

It should be noted that even the three different types (zero-, first-, second-order) of resonant regulators are plotted in Fig. 8, the first-order resonant regulator has been widely adopted [18] due to its significant frequency selection capability, thus it will be employed here to build the virtual impedance.

Based on above descriptions, the virtual impedance for the DFIG system high-frequency resonance damping can be obtained with the first-order resonant regulator and virtual components as the following:

1) PC + first-order resonant regulator, equals to, positive zero-order virtual impedance
2) NL + first-order resonant regulator, equals to, negative second-order virtual impedance

Case 1: PC + first-order resonant regulator, equals to, positive zero-order virtual impedance: As illustrated above, the PC manages to reduce the magnitude of the DFIG system impedance which behaves as an inductance unit. By combining the first-order resonant regulator together with the PC, the positive zero-order virtual impedance can be obtained. It needs to point out that, as plotted in Fig. 8, the proposed virtual impedance behaves as a PC within the frequency range lower than resonant frequency due to the 0° phase response, while it behaves as a negative capacitor within the frequency range higher than resonant frequency due to the −180° phase response.

The proposed virtual impedance with PC and first-order resonant regulator can be expressed as

$$Z_{\mathrm{PC}}(s)=\frac{\omega_c s}{s^2+\omega_c s+\omega_{\mathrm{reso}}^2}\frac{1}{sC_{\mathrm{xrsc}}}=\frac{\omega_c/C_{\mathrm{xrsc}}}{s^2+\omega_c s+\omega_{\mathrm{reso}}^2} \tag{8}$$

where Z_{PC} is the proposed virtual impedance with virtual PC, C_{xrsc} is the proposed virtual PC, ω_c is the resonant bandwidth parameter, and ω_{reso} is the resonant frequency.

Based on Fig. 5 and the PC + first-order resonant regulator virtual impedance, the reshaped impedance modeling can be obtained in Fig. 9. Since the Z_{PC} is implemented with the rotor current feedforward, the digital control delay and PWM update delay of total 1.5 sample periods also exists when introducing the virtual impedance. Inherently, this control delay is helpful to reduce the DFIG system phase response and increase the phase margin.

Thus, based on (8) and Fig. 9, the DFIG system impedance including the PC-based virtual impedance in the RSC can be presented as (9) shown at the bottom of the page where $H_{\mathrm{PC}}=R_r+Z_{L\sigma r}+Z_{\mathrm{RSC}}+Z_{\mathrm{PC}}G_d$.

Bode diagram of the DFIG system impedance $Z_{\mathrm{SYSTEM\_SR\_PC}}$ including the proposed virtual impedance $Z_{SR_{\mathrm{PC}}}$ with PC and first-order resonant regulator is plotted in Fig. 10, $\omega_c=5\ \mathrm{rad/s}$, $\omega_{\mathrm{reso}}=2\pi*1220\ \mathrm{rad/s}$, $C_{\mathrm{xrsc}}=0.08\ \mu\mathrm{F}$, control delay $=150\ \mu\mathrm{s}$. The control delay and slip are both taken into consideration in Fig. 10.

As shown in Fig. 10, when no effective virtual impedance is introduced as shown in cyan, the DFIG system impedance has a magnitude intersection point with the weak network impedance at the frequency around 1220 Hz, and the corresponding phase difference is 180°, resulting in a high-frequency resonance around 1220 Hz.

In contrast, when the virtual impedance of the PC is introduced in blue, the magnitude response of the DFIG system first decreases, then increases, and at last decreases again. This impedance reshaping ensures that only one single magnitude intersection at around 1210 Hz exists, and the phase difference at 1210 Hz is effectively reduced to around 142°, which guarantees the effective damping of the high-frequency resonance.

Nevertheless, if the negative capacitor is introduced, as shown in red, the magnitude response of the DFIG system first increases, then decreases, and at last increases again. As a result, there are three magnitude intersections at 1205, 1230, and 1245 Hz, respectively. As it can be observed, the intersection points at 1205 and 1245 Hz may still unfortunately cause resonance. This unfavorable phenomenon can also be explained as, the proposed virtual negative capacitor behaves as inductive units at the frequency range lower than resonant frequency, thus the DFIG system impedance magnitude will first increase; then the virtual negative capacitor behaves as capacitive units at the frequency range higher than resonant frequency, thus the DFIG system impedance magnitude will then decrease, just as shown in red in Fig. 10. Moreover, since the virtual negative capacitor behaves as capacitive units at the frequency range higher than resonant frequency, the DFIG system impedance phase concave between 1220 and 1240 Hz will be a consequence.

Thus, based on the above explanations, it can be found that the proposed virtual impedance of the PC + first-order resonant regulator is capable of appropriately reshaping the DFIG system impedance in order to mitigate the high-frequency resonance.

Case 2: NL + first-order resonant regulator, equals to, negative second-order virtual impedance

Obviously, the NL has similar influence on the DFIG system impedance as the PC, the combination of NL and first-order resonant regulator, which equals to the negative second-order virtual impedance, can be presented as

$$\begin{aligned} Z_{\mathrm{NL}}(s) &= \frac{\omega_c s}{s^2+\omega_c s+\omega_{\mathrm{reso}}^2}*(-sL_{\mathrm{xrsc}}) \\ &= \frac{-\omega_c L_{\mathrm{xrsc}} s^2}{s^2+\omega_c s+\omega_{\mathrm{reso}}^2} \end{aligned} \tag{10}$$

where, Z_{NL} is the proposed virtual impedance with NL, and $-L_{\mathrm{xrsc}}$ is the proposed NL.

The similar impedance reshaping result as shown in Fig. 9 can be obtained and is not given here for the sake of simplicity. Based on (10) and Fig. 9, the DFIG system impedance including the NL-based virtual impedance in RSC can be presented as (11) shown at the bottom of the page where $H_{\mathrm{NL}}=R_r+Z_{L\sigma r}+Z_{\mathrm{RSC}}+Z_{\mathrm{NL}}G_d$.

$$Z_{\mathrm{SYSTEM\_SR\_PC}}=\frac{Z_G Z_{\mathrm{SR\_PC}}}{Z_G+Z_{\mathrm{SR\_PC}}} \tag{9a}$$

$$Z_{\mathrm{SR\_PC}}=\frac{Z_{\mathrm{Lm}}H_{\mathrm{PC}}/\mathrm{slip}+(R_s+Z_{L\sigma s})H_{\mathrm{PC}}/\mathrm{slip}+Z_{\mathrm{Lm}}(R_s+Z_{L\sigma s})}{Z_{\mathrm{Lm}}+H_{\mathrm{PC}}/\mathrm{slip}} \tag{9b}$$

$$Z_{\mathrm{SYSTEM\_SR\_NL}}=\frac{Z_G Z_{\mathrm{SR\_NL}}}{Z_G+Z_{\mathrm{SR\_NL}}} \tag{11a}$$

$$Z_{\mathrm{SR\_NL}}=\frac{Z_{\mathrm{Lm}}H_{\mathrm{NL}}/\mathrm{slip}+(R_s+Z_{L\sigma s})H_{\mathrm{NL}}/\mathrm{slip}+Z_{\mathrm{Lm}}(R_s+Z_{L\sigma s})}{Z_{\mathrm{Lm}}+H_{\mathrm{NL}}/\mathrm{slip}} \tag{11b}$$

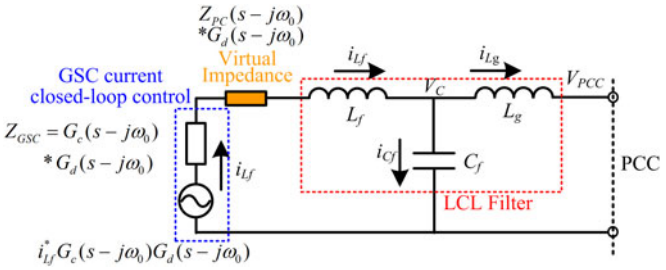

Fig. 11. Impedance modeling of GSC and *LCL* filter.

By adjusting the appropriate NL value to fit the equation of $1/(\omega_{\rm reso}C_{\rm xrsc})=\omega_{\rm reso}L_{\rm xrsc}$, $L_{\rm xrsc}=210$ mH, the same Bode diagram of the DFIG system impedance with virtual NL can be obtained, thus it will not be repeated here for the sake of simplicity.

It is important to clarify that the proposed virtual negative inductance value $L_{\rm xrsc}$ of 210 mH is reasonable and appropriate for the following two reasons. First, the digital control delay of 1.5 sample period will cause the transformation of virtual negative inductance to the combination of virtual negative inductance and negative resistance; as a consequence, the amplitude of virtual negative inductance will be multiplied with $cos(\omega_{\rm reso}T_d)=0.4$. Second, since the virtual negative inductance is implemented through rotor current feedforward, this means the virtual negative inductance is inserted in the DFIG rotor branch as shown in Fig. 9; thus, the amplitude of virtual negative inductance should be close to the DFIG mutual inductance of 79 mH in order to have an distinctive influence on the DFIG system impedance. The detailed theoretical explanation about these two reasons can be found in the following section of virtual impedance parameters design.

Based on the above explanations, it can be found that the introduced virtual PC and NL have the same influence on the DFIG system impedance from the perspective of impedance reshaping so as to mitigate the high-frequency resonance.

B. DFIG System Impedance Reshaping Through GSC

Obviously, the abovementioned two different kinds of virtual impedance can also be employed in GSC to reshape the DFIG system impedance. The introduced virtual impedance based on the PC can be presented the same as (8) and will not be described here.

Based on Fig. 11, the DFIG system impedance with the reshaped grid side impedance can be presented as (12) shown at the bottom of the page.

Fig. 12 shows the Bode diagram of the DFIG system impedance considering the proposed virtual impedance $Z_{\rm PC}$ with positive capacitor and first-order resonant regulator in the GSC, $\omega_c=5$ rad/s, $\omega_{\rm reso}=2\pi*1220$ rad/s, $C_{\rm xgsc}=0.5$ μF, control delay $=150$ μs.

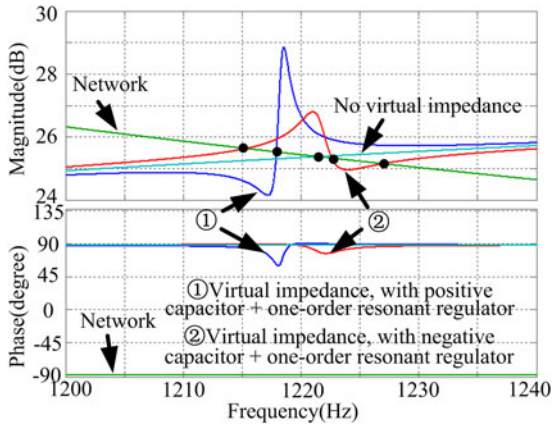

Fig. 12. Bode diagram of a DFIG system impedance considering the proposed virtual impedance $Z_{\rm PC}$ with positive capacitor and first-order resonant regulator in GSC, $\omega_c=5$ rad/s, $\omega_{\rm reso}=2\pi*1220$ rad/s, $C_{\rm xgsc}=0.5$ μF, control delay $=150$ μs.

The Bode diagram of (12) is very similar to Fig. 10. When the positive capacitor-based virtual impedance is employed (in blue), the magnitude intersection point moves from 1220 to 1217 Hz, and the phase difference also decreases from 180° to 151°. This means, through the effective impedance reshaping by the proposed virtual impedance in GSC, the original magnitude intersection point at 1220 Hz with the phase response of 180° can be successfully moved to the new magnitude intersection point at 1217 Hz with the phase response of 151°, thus the high-frequency resonance can be effectively mitigated.

Nevertheless, if the negative capacitor is adopted (in red), three intersection points at 1215, 1223, and 1227 Hz occur, and the high-frequency resonance of 1215 and 1227 Hz is still seen.

Clearly, when the NL, instead of the positive capacitor, is implemented, the high-frequency resonance can also be successfully eliminated if the NL value is appropriately tuned, thus it will not be described in detail here.

V. Virtual Impedance Parameters Design and Control Block Diagram

A. Parameter Design of Virtual Impedance for RSC and GSC Implementation

In order to achieve satisfactory damping of the high-frequency resonance, the parameter of the introduced virtual impedance needs to be carefully designed. The following discusses the positive capacitor and NL parameter design for the RSC and GSC implementation.

$$Z_{\rm SYSTEM\_G\_PC}=\frac{Z_{G\_PC}Z_{\rm SR}}{Z_{G\_PC}+Z_{\rm SR}} \tag{12a}$$

$$Z_{G\_PC}=\frac{Z_{\rm Cf}\left(Z_{\rm Lf}+Z_{\rm GSC}+Z_{\rm PC}G_d\right)+Z_{\rm Lg}\left(Z_{\rm Lf}+Z_{\rm GSC}+Z_{\rm PC}G_d\right)+Z_{\rm Cf}Z_{\rm Lg}}{Z_{\rm Cf}+\left(Z_{\rm Lf}+Z_{\rm GSC}+Z_{\rm PC}G_d\right)}. \tag{12b}$$

1) Parameter Design of Virtual Impedance for RSC: As shown in Fig. 9, the implementation of virtual impedance in the RSC only influences the rotor branch, and the rotor branch is in parallel connection with the mutual inductance branch. Thus, the paralleled impedance of the rotor branch and mutual inductance branch can be presented as (for the sake of clearer illustration, the NL is taken as an example)

$$Z_{\mathrm{RM}} = \frac{sL_m s\left(L_{\sigma r} - L_{\mathrm{xrsc}} e^{-\mathrm{sT}_d}\right)}{s\left(L_m + L_{\sigma r} - L_{\mathrm{xrsc}} e^{-\mathrm{sT}_d}\right)} \tag{13}$$

where the rotor resistance is small enough to be neglected, and the PI current regulator which contains the k_p part as resistance, and k_i part as capacitance, can also be neglected due to its small value of k_p and k_i.

It is clear that in order to reshape the inherent inductive nature of the DFIG system impedance, the Z_{RM} needs to become capacitive with its magnitude as large as possible, so the denominator of (13) needs to be as small as possible. According to the Euler equation, the denominator of (13) can be rewritten as

$$\begin{aligned} L_m + L_{\sigma r} - L_{\mathrm{xrsc}} e^{-\mathrm{sT}_d} = {} & L_m + L_{\sigma r} - L_{\mathrm{xrsc}} \left(\cos(\omega_{\mathrm{reso}} T_d)\right. \\ & \left. - j \sin(\omega_{\mathrm{reso}} T_d)\right) \end{aligned} \tag{14}$$

where T_d is the digital control delay.

By assuming the following equation, the largest equivalent capacitive impedance of Z_{RM} in (13) can be obtained as

$$L_{\mathrm{xrsc}} = (L_m + L_{\sigma r})/\cos(\omega_{\mathrm{reso}} T_d). \tag{15}$$

By substituting the parameters given in Table I, the optimized value of the virtual impedance for RSC damping implementation can be calculated as a NL of -206 mH (the reasons for this large inductance value is given below Fig. 10) or the positive capacitor of 0.08 μF. This calculation result has been used to plot the Bode diagram of DFIG system impedance with the introduction of virtual impedance in Fig. 10, and it is shown that the original resonance of 1220 Hz can be well eliminated, and the magnitude intersection point shifts to 1210 Hz with the phase difference of 142°.

It can be also found from (15) that the optimized virtual impedance parameter for RSC is determined by mutual inductance L_m, rotor leakage inductance $L_{\sigma r}$, resonance frequency ω_{reso}, and control delay T_d.

2) Parameter Design of Virtual Impedance for GSC: Similar deduction can be adopted to obtain the optimized parameter of virtual impedance for the GSC.

According to Fig. 11, the implementation of virtual impedance in the GSC only influences the converter branch, and the filter capacitor is in parallel connection with the converter branch.

Thus, the paralleled impedance of the converter branch and the filter capacitor can be presented as (for the sake of clearer illustration, the negative inductance is taken as an example)

$$Z_{\mathrm{GC}} = \frac{\frac{1}{C_f}\left(L_f - L_{\mathrm{xgsc}} e^{-\mathrm{sT}_d}\right)}{\frac{1}{sC_f} + s\left(L_f - L_{\mathrm{xgsc}} e^{-\mathrm{sT}_d}\right)} \tag{16}$$

where the PI current regulator which contains the k_p part as resistance and k_i part as capacitance can be neglected due to its small value of k_p and k_i.

In order to make the Z_{GC} a capacitive unit with its magnitude as large as possible, the denominator of (16) needs to be as small as possible. According to the Euler equation, the denominator of (16) can be rewritten as

$$\begin{aligned} \frac{1}{sC} + s\left(L_1 - L_{\mathrm{xgsc}} e^{-\mathrm{sT}_d}\right) = {} & \frac{1}{sC} + s\left(L_1\right. \\ & \left. - L_{\mathrm{xgsc}} \left(\cos(\omega_{\mathrm{reso}} T_d) - j \sin(\omega_{\mathrm{reso}} T_d)\right)\right). \end{aligned} \tag{17}$$

By assuming the following equation, the largest equivalent capacitive impedance of Z_{GC} in (16) can be obtained as

$$L_{\mathrm{xgsc}} = \left(L_1 - 1/\omega_{\mathrm{reso}}^2 C\right)/\cos(\omega_{\mathrm{reso}} T_d). \tag{18}$$

By substituting the parameters given in Table I, the optimized value of virtual impedance for GSC damping implementation can be calculated as a NL of -34 mH or the positive capacitor of 0.5 μF. This result has been used to plot the Bode diagram of the DFIG system impedance with the introduction of virtual impedance in Fig. 12, and it is shown that the original resonance of 1220 Hz can be well eliminated, and the magnitude intersection point shifts to 1217 Hz with the phase difference of 151°.

It can be also found from (18) that the optimized virtual impedance parameter for GSC is determined by converter-side inductor filter L_f, capacitor filter C_f, resonance frequency ω_{reso}, and control time delay T_d.

In conclusion, by comparing the reshaped DFIG system impedance with the virtual impedance as shown in Figs. 10 and 12, it can be found that the active damping in RSC with virtual impedance has a larger phase margin of 38° than the that of GSC with a virtual impedance of 29°; thus, better high-frequency resonance damping can be achieved if the virtual impedance damping is implemented in RSC control.

B. Control Block Diagram

Fig. 13 shows the control block diagram of the proposed DFIG system high-frequency resonance damping control strategy using virtual impedance of PC or NL, and this strategy can be implemented in either RSC or GSC.

As it can be seen, for the RSC control, since the occurrence of DFIG system high-frequency resonance will pollute the stator voltage with high-frequency components higher than 1 kHz, an enhanced PLL module integrated with low-pass filter can be used to provide the information of grid voltage fundamental synchronous angular speed ω_1 and phase angle θ_1, while the encoder gives out the DFIG rotor position θ_r and speed ω_r. The rotor current $\boldsymbol{I}_{\mathrm{rdq}}^{+}$ is first sampled and then regulated with PI regulator to output the harvested wind energy.

The resonance frequency detection unit employs an ANF and frequency-locked loop (FLL) to detect and output the resonance frequency ω_{reso} [22]. The ANF unit is responsible to extract the resonance component, while the FLL unit is responsible to identify the frequency of the resonance component. Then, the proposed virtual impedance with positive capacitor or NL can be

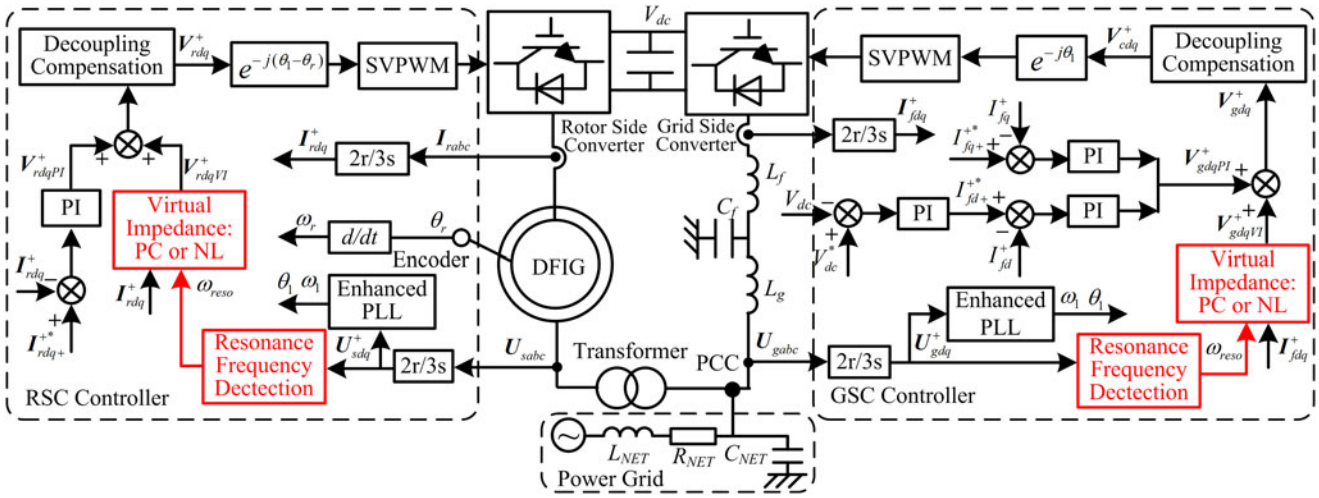

Fig. 13. Control block diagram of the proposed DFIG system high-frequency resonance damping control strategy using virtual impedance of PC or NL.

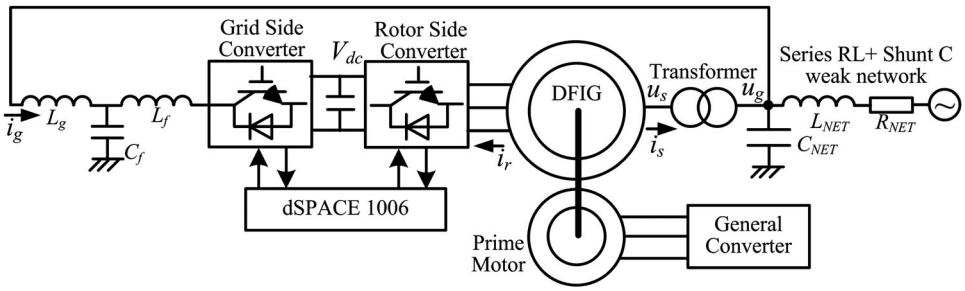

Fig. 14. Setup of a 7.5-kW DFIG system test rig.

flexibly adjusted based on various resonance frequencies. The introduction of virtual impedance does not require rotor current closed-loop control, but it can be regarded as rotor current feedforward component. Then, the output of the rotor current PI closed-loop control $\boldsymbol{V}^{+}_{\mathrm{rdqPI}}$, the output of virtual impedance $\boldsymbol{V}^{+}_{\mathrm{rdqVI}}$ and the decoupling compensation are added together as the rotor control voltage $\boldsymbol{V}^{+}_{\mathrm{rdq}}$, which is then transformed to the rotor stationary frame and delivered as an input of the space vector PWM.

The GSC control can similarly be implemented as the RSC control. The dc-link voltage is well regulated by PI regulator, and its output is delivered as L_{f} filter current d-axis component reference $I^{+*}_{\mathrm{fd+}}$, then the L_f filter current I_{fdq} is regulated also by the PI regulator. The virtual impedance in the GSC can be similarly introduced, and no L_f filter current closed-loop is required for the virtual impedance introduction, but only the L_f filter current feedforward with the virtual impedance is needed.

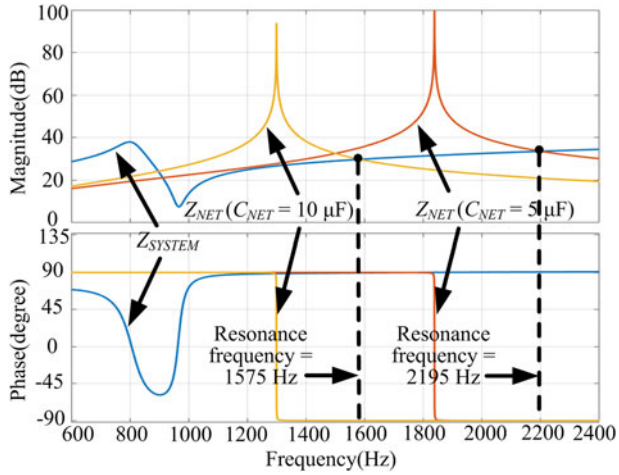

Fig. 15. Bode diagram of a DFIG system impedance and series RL + shunt C network impedance with $C_{\mathrm{NET}} = 10,\ 5\ \mu\mathrm{F}$, $R_{\mathrm{NET}} = 3\ \mathrm{m\Omega}$, $L_{\mathrm{NET}} = 1.5\ \mathrm{mH}$.

VI. Experimental Validation

A. Experimental Setup

In order to validate the correctness of the proposed active damping strategy of DFIG system high-frequency resonance implemented in either RSC or GSC, experimental setup is built up.

A downscaled 7.5-kW test rig is used and the overall system is shown in Fig. 14. The experimental DFIG system parameters can be found in Table I. The weak network is simulated using three-phase inductors and capacitors. The DFIG is externally driven by a prime motor, and two 5.5-kW Danfoss motor drives are used for the GSC and the RSC, both of which

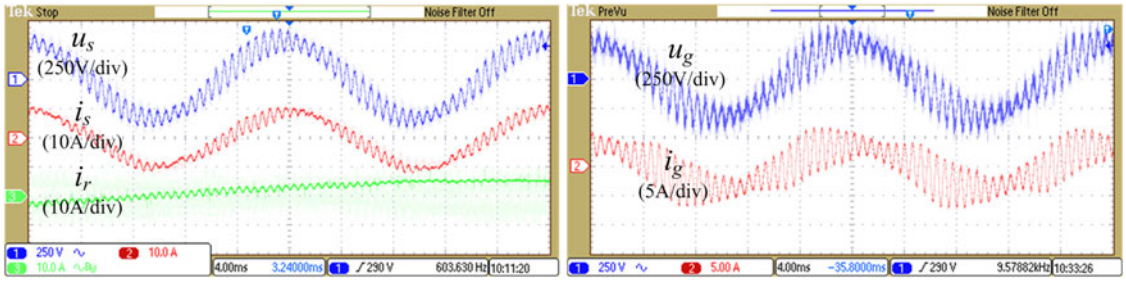

Fig. 16. No active damping strategy, weak network parameters of $R_{\mathrm{NET}} = 3\ \mathrm{m}\Omega$, $L_{\mathrm{NET}} = 1.5\ \mathrm{mH}$, $C_{\mathrm{NET}} = 10\ \mu\mathrm{F}$.

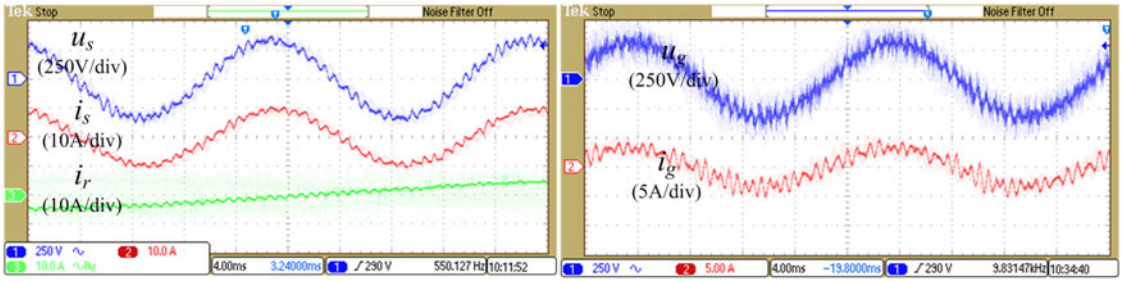

Fig. 17. Steady-state response when active damping strategy in RSC is enabled, weak network parameters of $R_{\mathrm{NET}} = 3\ \mathrm{m}\Omega$, $L_{\mathrm{NET}} = 1.5\ \mathrm{mH}$, $C_{\mathrm{NET}} = 10\ \mu\mathrm{F}$.

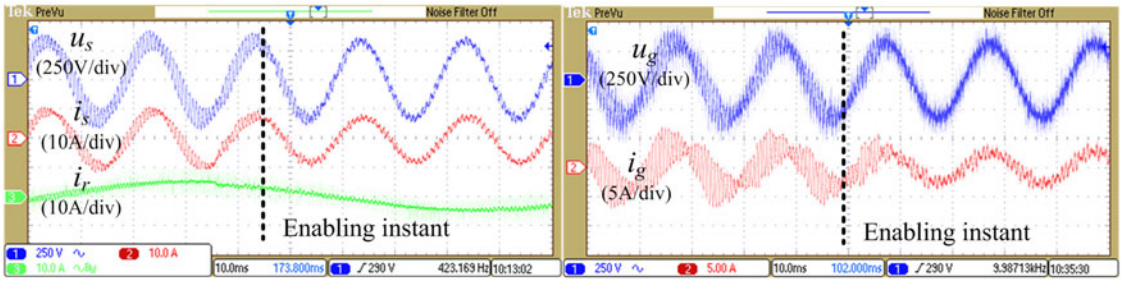

Fig. 18. Transient state response when active damping strategy in RSC is enabled, weak network parameters of $R_{\mathrm{NET}} = 3\ \mathrm{m}\Omega$, $L_{\mathrm{NET}} = 1.5\ \mathrm{mH}$, $C_{\mathrm{NET}} = 10\ \mu\mathrm{F}$.

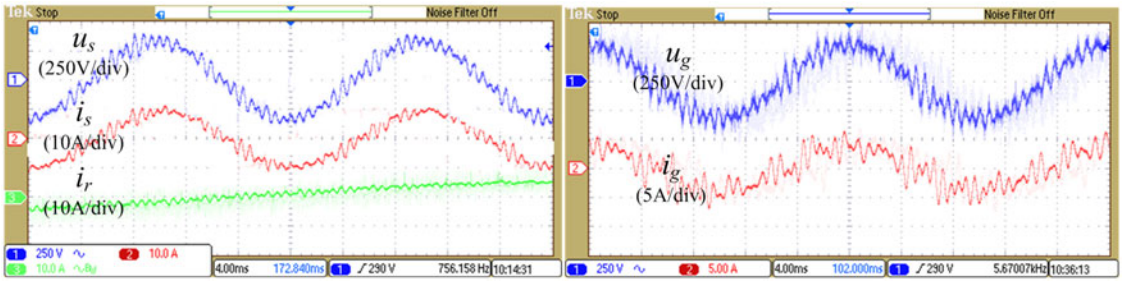

Fig. 19. Steady-state response when active damping strategy in GSC is enabled, weak network parameters of $R_{\mathrm{NET}} = 3\ \mathrm{m}\Omega$, $L_{\mathrm{NET}} = 1.5\ \mathrm{mH}$, $C_{\mathrm{NET}} = 10\ \mu\mathrm{F}$.

are controlled with dSPACE 1006. The rotor speed is set 1200 r/min (0.8 p.u.), with the synchronous speed of 1500 r/min (1.0 p.u.). The DFIG system output power is set at 5 kW. The dc-link voltage is 650 V. The sample frequency f_s and switching frequency f_{sw} for both RSC and GSC is 10 and 5 kHz, respectively. The weak network parameters are $R_{\mathrm{NET}} = 3\ \mathrm{m}\Omega$, $L_{\mathrm{NET}} = 1.5\ \mathrm{mH}$, $C_{\mathrm{NET}} = 10\ \mu\mathrm{F}$.

During the experimental validation process, the prime motor is driven by the general converter which will unfortunately inject high-frequency switching noise to the power grid; as a consequence, the u_g in all the experiment results Figs. 16–24 will contain switching noise due to the weak power grid impedance. This switching noise can be filtered out by the transformer leakage inductance, thus the stator voltage u_s in all the experiment

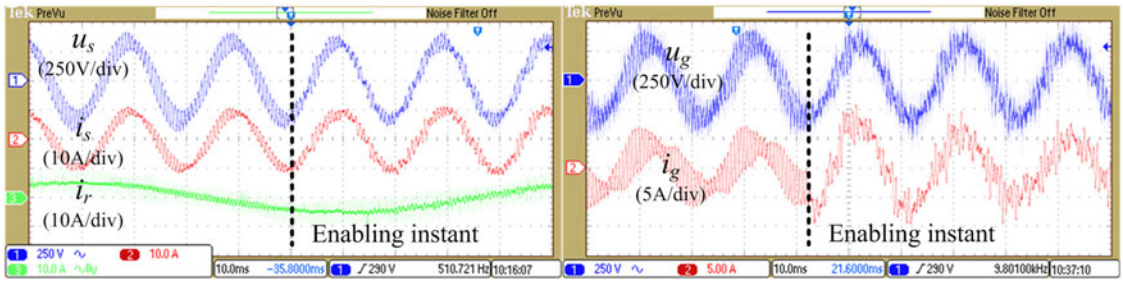

Fig. 20. Transient state response when active damping strategy in GSC is enabled, weak network parameters of $R_{\rm NET} = 3\ \mathrm{m\Omega}$, $L_{\rm NET} = 1.5\ \mathrm{mH}$, $C_{\rm NET} = 10\ \mu\mathrm{F}$.

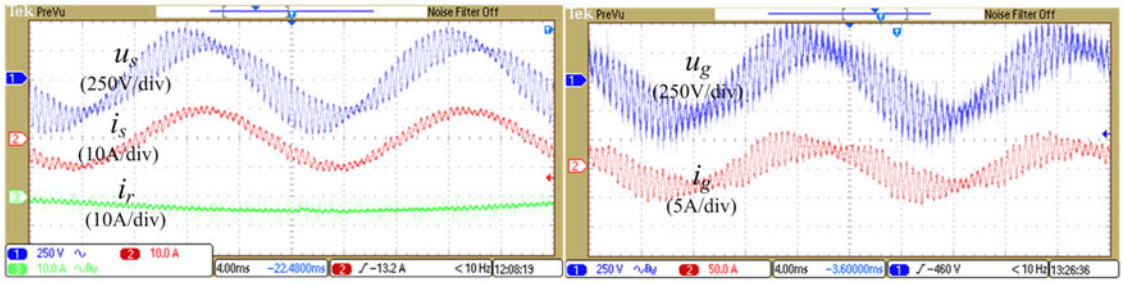

Fig. 21. Experimental result of a DFIG system when shunt capacitance $C_{\rm NET} = 5\ \mu\mathrm{F}$ in the weak grid network, $R_{\rm NET} = 3\ \mathrm{m\Omega}$, $L_{\rm NET} = 1.5\ \mathrm{mH}$, no active damping strategy.

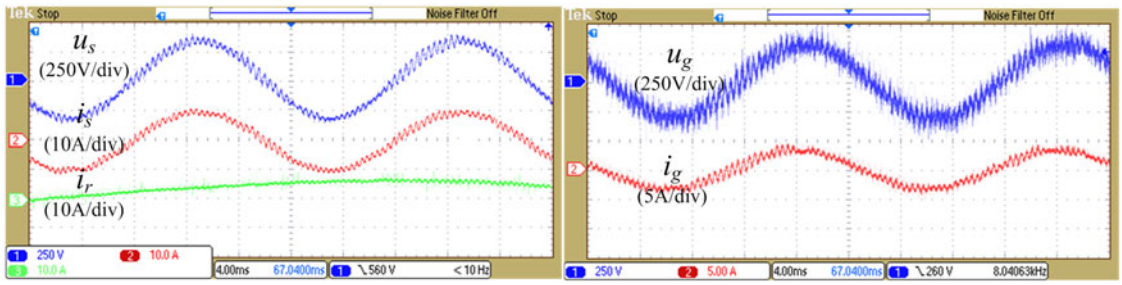

Fig. 22. Steady-state response when active damping strategy in RSC is enabled, weak network parameters of $R_{\rm NET} = 3\ \mathrm{m\Omega}$, $L_{\rm NET} = 1.5\ \mathrm{mH}$, $C_{\rm NET} = 5\ \mu\mathrm{F}$.

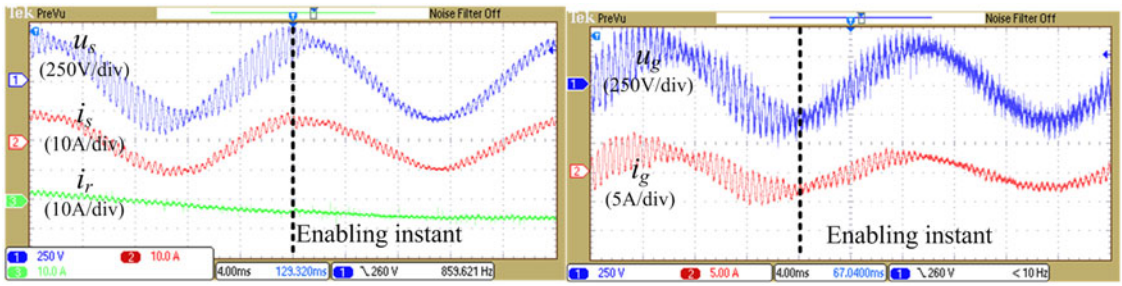

Fig. 23. Transient state response when active damping strategy in RSC is enabled, weak network parameters of $R_{\rm NET} = 3\ \mathrm{m\Omega}$, $L_{\rm NET} = 1.5\ \mathrm{mH}$, $C_{\rm NET} = 5\ \mu\mathrm{F}$.

results do not contain the noise. Considering that this noise does not influence the resonance active damping performance, the experimental results are still valid to validate the active damping method.

The Bode diagrams of the DFIG system impedance and the parallel compensated weak network impedance ($R_{\rm NET} = 3\ \mathrm{m\Omega}$, $L_{\rm NET} = 1.5\ \mathrm{mH}$, $C_{\rm NET} = 10,\ 5\ \mu\mathrm{F}$) are plotted in Fig. 15. As it can be seen, the theoretical analysis shows that the high-frequency resonance of 1575 and 2195 Hz will occur due to the phase difference of 180 between network impedance $Z_{\rm NET}$ and DFIG system impedance $Z_{\rm SYSTEM}$ when the network shunt capacitance $C_{\rm NET} = 10,\ 5\ \mu\mathrm{F}$, respectively.

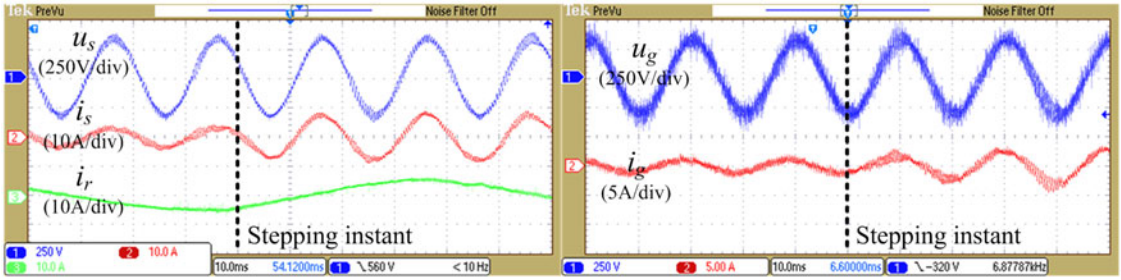

Fig. 24. Transient state response of DFIG stator output power stepping from 0.5 to 1.0 p.u. when active damping strategy in RSC is enabled, weak network parameters of $R_{\mathrm{NET}} = 3\ \mathrm{m}\Omega$, $L_{\mathrm{NET}} = 1.5\ \mathrm{mH}$, $C_{\mathrm{NET}} = 5\ \mu\mathrm{F}$.

B. Experimental Results

Fig. 16 shows the experimental result of the DFIG system when no effective active damping control strategy is implemented. Clearly, the high-frequency resonance around 1600 Hz, which matches well with the theoretical analysis results shown in Fig. 15, will occur in three-phase stator voltage and current, rotor current, grid-side voltage, and current as a consequence of impedance interaction between the DFIG system and the parallel compensated weak network grid.

Fig. 17 shows the experimental result of the DFIG system when the proposed active damping control strategy is implemented in the RSC by the rotor current feedforward method. By comparing the experimental results shown in Figs. 16 and 17, it can be explicitly found that the high-frequency resonance can be effectively damped in all the stator voltage and current, grid-side voltage, and current. Therefore, the effectiveness of the proposed active damping strategy implemented in the RSC can be validated based on the experimental results.

Moreover, the experimental result of transient response at the enabling instant of the active damping strategy in RSC is also provided in Fig. 18. As it can be observed, once the damping is enabled, the high-frequency resonance components in the stator voltage and current, as well as the grid-side voltage and current can be mitigated within around 10 ms, which verifies the fast dynamic response capability of the proposed active damping method.

Similarly, the active damping strategy can also be implemented in GSC, with the converter-side current feedforward method. According to Fig. 19, when the active damping strategy in GSC is enabled, the high-frequency resonance components can also be mitigated. However, it should be noted that the active damping performance when GSC is involved as shown in Fig. 19 is poorer than the active damping performance when the RSC is involved as shown in Fig. 17. According to the theoretical analysis conducted in Section IV, this difference is because that the RSC with the virtual impedance has a larger phase margin of 38° than the GSC with the virtual impedance of 29°; thus, a better high-frequency resonance damping can be achieved if the virtual impedance damping is implemented in RSC control, which validates the correctness of the analysis results given in Figs. 10 and 12.

Fig. 20 shows also the experimental result of transient response at the enabling instant of active damping strategy in the GSC. Similar as in Fig. 18, once the damping is enabled, the fast dynamic response of active damping can be achieved within around 10 ms, which also verifies the fast dynamic response capability of the proposed active damping strategy.

TABLE II
HIGH-FREQUENCY RESONANCE ACCORDING TO THEORETICAL ANALYSIS AND EXPERIMENTAL RESULTS

Shunt Capacitor	Theoretical Analysis	Experimental Results	
		Active damping disabled	Active damping enabled
10 μF	1575 Hz	1600 Hz u_s 28.5%	1600 Hz u_s 6.7%
5 μF	2195 Hz	2250 Hz u_s 38.7%	2250 Hz u_s 8.6%

In order to further validate the effectiveness of the proposed active damping strategy, the experimental results under weak network parameters of $R_{\mathrm{NET}} = 3\ \mathrm{m}\Omega$, $L_{\mathrm{NET}} = 1.5\ \mathrm{mH}$, $C_{\mathrm{NET}} = 5\ \mu\mathrm{F}$ are also provided. As a result of the network shunt capacitance changing from 10 to 5 μF, the high-frequency resonance frequency changes from 1600 to 2250 Hz as shown in Fig. 21, and this resonance frequency is also close to the theoretical analysis result of 2195 Hz in Fig. 15 and Table II.

Similarly, when active damping strategy in RSC is enabled as shown in Fig. 22, the resonance can be effectively mitigated both in stator voltage/current, rotor current, and grid-side current. Besides, the transient state response at the enabling instant of the active damping strategy in RSC is also given in Fig. 23, it can be observed that the active damping strategy is capable of mitigating the resonance within around 10 ms, which ensures its fast dynamic response capability.

Fig. 24 shows the transient response when the DFIG stator output active power steps from 0.5 to 1.0 p.u. Clearly, the active damping strategy remains effective within the entire stepping transient period, and the output active power steps within around 10 ms, which guarantees the excellent control capability of the delivered wind power to the grid. Most importantly, this experimental result is able to validate the effectiveness of the proposed damping strategy under practical application where the output wind power may always in variation.

Thus, based on the experimental results shown above, it can be concluded that the proposed theoretical analysis on the high-frequency resonance frequency is accurate, and the proposed

active damping strategy implemented in either RSC or GSC is effective under practical application situation, i.e., under different weak network parameters (mainly with different network shunt capacitance in variation), as well as different stator output wind power, these advantages make the proposed active damping strategy reliable and effective in the real-world wind power generation applications. Besides, the active damping strategy implemented in the RSC has a better performance than being implemented in GSC due to the larger phase margin, thus the active damping in RSC is preferred.

VII. Conclusion

This paper has focused on the active damping control strategy for the DFIG system under parallel compensated weak network. The active damping strategy can be implemented in either RSC or GSC to reshape the overall DFIG system impedance.

1) The original high-frequency resonance can be damped by decreasing the phase difference with the virtual negative inductor or positive capacitor to produce an acceptable phase margin.
2) The rotor current feedforward in the RSC and converter-side current feedforward in GSC is proposed to introduce the virtual impedance and achieve the active damping performance.
3) Experimental results have validated the acceptable steady-state active damping performance, and also the fast dynamic response capability of the proposed active damping strategy.
4) Both theoretical analysis and experimental results verify that better active damping performance can be ensured if the active damping strategy is implemented in the RSC rather than GSC.

References

[1] F. Blaabjerg, and K. Ma, "Future on power electronics for wind turbine systems," *IEEE J. Emerg. Sel. Topics Power Electron.*, vol. 1, no. 3, pp. 139–152, Sep. 2013.

[2] K. Ma, L. Tutelea, I. Boldea, D. M. Ionel, and F. Blaabjerg, "Power electronic drives, controls, and electric generators for large wind turbines—An overview," *Electr. Power Compon. Syst.*, vol. 43, no. 12, pp. 1406–1421, 2015.

[3] H. Nian, P. Cheng, and Z. Q. Zhu, "Independent operation of DFIG-based WECS using resonant feedback compensators under unbalanced grid voltage conditions," *IEEE Trans. Power Electron.*, vol. 30, no. 7, pp. 3650 –3661, Jul. 2015.

[4] H. Nian, P. Cheng, and Z. Q. Zhu, "Coordinated direct power control of DFIG system without phase-locked loop under unbalanced grid voltage conditions," *IEEE Trans. Power Electron.*, vol. 31, no. 4, pp. 2905–2918, Apr. 2016.

[5] D. Zhou, F. Blaabjerg, T. Franke, M. Lau, and M. Tonnes, "Reduced cost of reactive power in doubly fed induction generator wind turbine system with optimized grid filter," *IEEE Trans. Power Electron.*, vol. 30, no. 10, pp. 5581–5590, Oct. 2015.

[6] D. Zhou, F. Blaabjerg, T. Franke, M. Tonnes, and M. Lau, "Optimized reactive power flow of DFIG power converters for better reliability performance considering grid codes," *IEEE Trans. Ind. Electron.*, vol. 62, no. 3, pp. 1552–1562, Mar. 2015.

[7] I. Vieto and J. Sun, "Impedance modeling of doubly-fed induction generators," in *Proc. Power Electron. Appl. ECCE Eur.*, Sep. 2015, pp. 1–10.

[8] I. Vieto and J. Sun, "Damping of subsynchronous resonance involving type-III wind turbines," in *Proc. Control Modeling Power Electron.*, 2015, pp. 1–8.

[9] I. Vieto and J. Sun, "Small-signal impedance modelling of type-III wind turbine," in *Proc. Power Energy Society Gen. Meet.*, 2015, pp. 1–5.

[10] I. Vieto and J. Sun, "Real-time simulation of subsynchronous resonance in type-III wind turbines," in *Proc. Control Modeling Power Electron.*, 2014, pp. 1–8.

[11] Z. Miao, "Impedance-model-based SSR analysis for type 3 wind generator and series-compensated network," *IEEE Trans. Energy Convers.*, vol. 27, no. 4, pp. 984–991, Dec. 2012.

[12] L. Piyasinghe, Z. Miao, J. Khazaei, and L. Fan, "Impedance model-based SSR analysis for TCSC compensated type-3 wind energy delivery systems," *IEEE Trans. Sustainable Energy.*, vol. 6, no. 1, pp. 179–187, Jan. 2015.

[13] L. Fan and Z. Miao, "Nyquist-stability-criterion-based SSR explanation for type-3 wind generators," *IEEE Trans. Energy Convers.*, vol. 27, no. 3, pp. 807–809, Sep. 2012.

[14] L. Fan and Z. Miao, "Mitigating SSR using DFIG-based wind generation," *IEEE Trans. Sustainable Energy*, vol. 3, no. 3, pp. 349–358, Jul. 2012.

[15] X. Wang, F. Blaabjerg, and P. C. Loh, "Grid-current-feedback active damping for LCL resonance in grid-connected voltage source converters," *IEEE Trans. Power Electron.*, vol. 31, no. 1, pp. 213–223, Jan. 2016.

[16] X. Wang, Y. Pang, P. C. Loh, and F. Blaabjerg, "A series-LC-filtered active damper with grid disturbance rejection for AC power-electronics-based power systems," *IEEE Trans. Power Electron.*, vol. 30, no. 8, pp. 4037–4041, Aug. 2015.

[17] X. Wang, F. Blaabjerg, and P. C. Loh, "Virtual RC damping of LCL-filtered voltage source converters with extended selective harmonic compensation," *IEEE Trans. Power Electron.*, vol. 30, no. 9, pp. 4726–4737, Sep. 2015.

[18] X. Wang, F. Blaabjerg, and Z. Chen, "Synthesis of variable harmonic impedance in inverter-interfaced distributed generation unit for harmonic damping throughout a distribution network," *IEEE Trans. Ind. Appl.*, vol. 48, no. 4, pp. 1407–1417, Jul./Aug. 2012.

[19] X. Wang, F. Blaabjerg, and Z. Chen, "Autonomous control of inverter interfaced distributed generation units for harmonic current filtering and resonance damping in an islanded microgrid," *IEEE Trans. Ind. Appl.*, vol. 50, no. 1, pp. 452–461, Jan./Feb. 2014.

[20] X. Wang, F. Blaabjerg, and W. Wu, "Modeling and analysis of harmonic stability in an AC power-electronics-based power system," *IEEE Trans. Power Electron.*, vol. 29, no. 12, pp. 6421–6432, Dec. 2014.

[21] X. Wang, F. Blaabjerg, M. Liserre, Z. Chen, J. He, and Y. Li, "An active damper for stabilizing power-electronics-based AC systems," *IEEE Trans. Power Electron.*, vol. 29, no. 7, pp. 3318–3329, Jul. 2014.

[22] X. Wang, F. Blaabjerg, and M. Liserre, "An active damper to suppress multiple resonances with unknown frequencies," in *Proc. Appl. Power Electron. Conf. Expo.*, 2014, pp. 2184–2194.

[23] X. Wang, Y. Li, F. Blaabjerg, and P. C. Loh, "Virtual-impedance-based control for voltage-source and current-source converters," *IEEE Trans. Power Electron.*, vol. 30, no. 12, pp. 7019–7037, Dec. 2015.

[24] C. Wan, M. Huang, C. K. Tse, and X. Ruan, "Effects of interaction of power converters coupled via power grid: A design-oriented study," *IEEE Trans. Power Electron.*, vol. 30, no. 7, pp. 3589–3600, Jul. 2015.

[25] X. Wang, C. Bao, X. Ruan, W. Li, and D. Pan, "Design considerations of digitally controlled LCL-filtered inverter with capacitor current-feedback active damping," *IEEE J. Emerg. Sel. Topics Power Electron.*, vol. 2, no. 4, pp. 972–984, Dec. 2014.

[26] C. Bao, X. Ruan, X. Wang, W. Li, D. Pan, and K. Weng, "Step-by-step controller design for LCL-type grid-connected inverter with capacitor-current-feedback active-damping," *IEEE Trans. Power Electron.*, vol. 29, no. 3, pp. 1239–1253, Mar. 2014.

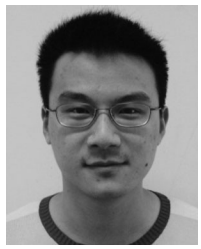

Yipeng Song was born in Hangzhou, China. He received the B.Sc. and Ph.D. degrees from the College of Electrical Engineering, Zhejiang University, Hangzhou, in 2010 and 2015, respectively.

He is currently working as a Postdoctoral Researcher at the Department of Energy Technology, Aalborg University, Aalborg, Denmark. His current research interests include motor control with power electronics devices in renewable-energy conversion, particularly the control and operation of doubly fed induction generators for wind power generation.

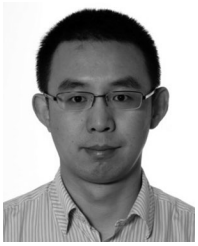

Xiongfei Wang (S'10–M'13) received the B.S. degree in electrical engineering from Yanshan University, Qinhuangdao, China, in 2006, the M.S. degree in electrical engineering from the Harbin Institute of Technology, Harbin, China, in 2008, and the Ph.D. degree from Aalborg University, Aalborg, Denmark, in 2013.

Since 2009, he has been with the Aalborg University, where he is currently an Assistant Professor at the Department of Energy Technology. His research interests include modeling and control of grid-connected converters, harmonics analysis and control, passive and active filters, and stability of power electronic-based power systems.

Dr. Wang received an IEEE Power Electronics Transactions Prize Paper award in 2014. He serves as the Associate Editor of the IEEE TRANSACTIONS ON INDUSTRY APPLICATIONS and the Guest Associate Editor of the IEEE JOURNAL OF EMERGING AND SELECTED TOPICS IN POWER ELECTRONICS Special Issue on Distributed Generation.

Frede Blaabjerg (S'86–M'88–SM'97–F'03) was a Ph.D. Student with Aalborg University, Aalborg, Denmark, from 1988 to 1992.

He was with ABB-Scandia, Randers, Denmark, from 1987 to 1988. He became an Assistant Professor in 1992, an Associate Professor in 1996, and a Full Professor of power electronics and drives in 1998. His current research interests include power electronics and its applications, such as in wind turbines, PV systems, reliability, harmonics, and adjustable speed drives.

Dr. Blaabjerg received 17 IEEE Prize Paper Awards, the IEEE PELS Distinguished Service Award in 2009, the EPE-PEMC Council Award in 2010, the IEEE William E. Newell Power Electronics Award in 2014, and the Villum Kann Rasmussen Research Award in 2014. He was an Editor-in-Chief of the IEEE TRANSACTIONS ON POWER ELECTRONICS from 2006 to 2012. He was nominated in 2014 and 2015 by Thomson Reuters to be between the most 250 cited researchers in Engineering in the world.